

# Scanning Ion Conductance Microscopy

Chiao-Chen Chen, Yi Zhou, and Lane A. Baker

Department of Chemistry, Indiana University, Bloomington, Indiana 47405;  
email: lanbaker@indiana.edu

Annu. Rev. Anal. Chem. 2012. 5:207–28

First published online as a Review in Advance on  
April 9, 2012

The *Annual Review of Analytical Chemistry* is online  
at [anchem.annualreviews.org](http://anchem.annualreviews.org)

This article's doi:  
10.1146/annurev-anchem-062011-143203

Copyright © 2012 by Annual Reviews.  
All rights reserved

1936-1327/12/0719-0207\$20.00

## Keywords

nanopipette, SICM, scanning probe microscopy, microscopy, bioanalytical

## Abstract

Scanning ion conductance microscopy (SICM) is a versatile type of scanning probe microscopy for studies in molecular biology and materials science. Recent advances in feedback and probe fabrication have greatly increased the resolution, stability, and speed of imaging. Noncontact imaging and the ability to deliver materials to localized areas have made SICM especially fruitful for studies of molecular biology, and many examples of such use have been reported. In this review, we highlight new developments in the operation of SICM and describe some of the most exciting recent studies from this growing field.

**SICM:** scanning ion conductance microscopy/microscope

## 1. INTRODUCTION

Scanning ion conductance microscopy (SICM), a scanning probe technique, utilizes a nanopipette to scan samples bathed in electrolytic solutions (**Figure 1**). The operation of SICM relies on an ion current that flows between an electrode inside a pipette and another electrode in an external bath solution. This ion current, which is highly dependent on the tip-sample separation, is utilized as a feedback signal to maintain the tip-sample separation and to allow the pipette to follow surface contours, which generates topographic information. SICM has attracted significant attention due to potential applications with living cells, in which high-resolution, noncontact imaging proves beneficial. This review summarizes probe properties, scanning mechanisms, and significant applications of SICM. We review research from the original development of this technique in 1989 (1) up to the latest progress.

## 2. PRINCIPLES OF OPERATION AND INSTRUMENTATION

SICM was originally developed in 1989 by Hansma et al. (1) to image nonconductive surfaces immersed in electrolytic solution. Improved feedback techniques (2–6), which allow robust and high-speed scanning, further demonstrate the ability to image delicate cellular structures without damaging the sample and thus are significantly advancing the opportunities for experimentation with SICM.

**Figure 1a** illustrates SICM. The SICM probe—an electrolyte-filled nanopipette with an Ag/AgCl electrode inserted from the back—is placed in an electrolyte solution, and a bias is applied between the pipette electrode and a reference electrode in solution. Under the applied bias, ions flow between the pipette electrode and the reference electrode (through the pipette tip) to generate an ion current ( $I$ ). The magnitude of ion currents is determined by the total resistance

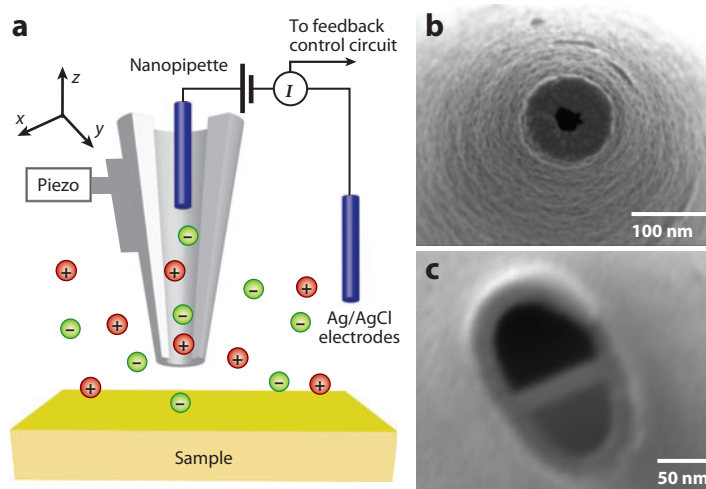


**Figure 1**

Illustration of a scanning ion conductance microscope (SICM). (a) A nanopipette filled with electrolyte is brought in proximity to a sample of interest. A bias applied between an electrode in the pipette and another electrode in the bulk solution generates an ion current, which can be used in feedback control. The nanopipette is mounted on a piezoelectric positioner, which controls the movement of the nanopipette. (b,c) Scanning electron micrographs of (b) a single-barrel nanopipette (~60 nm inner diameter) and (c) a  $\theta$  pipette (~50 nm inner diameter in both barrels). Such pipettes can serve as probes in SICM.

of the pipette ( $R_T$ ), a combination of the pipette resistance ( $R_p$ ), and the access resistance between the pipette tip and the sample surface ( $R_{ac}$ ), which can be described mathematically (7).

Pipette resistance can be calculated geometrically with Equation 1, where  $r_i$  is the inner radius of the tip opening,  $r_p$  is the inner radius of the tip base,  $b$  is the tip length, and  $\kappa$  is the conductivity of the electrolyte in the pipette. Although pipette resistance is constant for pipettes with the same geometry, access resistance is strongly affected by the distance ( $d$ ) between the tip and the sample. A mathematical description of  $R_{ac}$  is given by Equation 2, where  $r_o$  is the outer radius of the tip opening. The magnitude of ion currents can be determined from the applied potential ( $U$ ) and the overall resistance of a pipette ( $R_T$ ) with Equation 3, which demonstrates the dependence of ion currents on tip-sample distances:

$$R_p = \frac{b}{\kappa \cdot \pi \cdot r_p \cdot r_i}; \quad (1)$$

$$R_{ac} \approx \frac{\frac{3}{2} \ln(\frac{r_o}{r_i})}{\kappa \cdot \pi \cdot d}; \quad (2)$$

$$I(d) = \frac{U}{R_T} = \frac{U}{R_p + R_{ac}} \approx I_{MAX} \left( 1 + \frac{\frac{3}{2} \ln(\frac{r_o}{r_i}) \cdot r_p \cdot r_i}{b \cdot d} \right)^{-1}; \quad I_{MAX} = \frac{U}{R_p}. \quad (3)$$

This current-distance relationship can be observed in the form of an approach curve (**Figure 2d**).

In an approach curve, the ion current is at the maximum value ( $I_{MAX}$ ) when the pipette is far away from the sample surface. As the pipette approaches very close to the sample surface, ion flow is impeded and thus causes a rapid decrease in the ion current. The distance-dependent current measured by the pipette provides feedback to control tip-sample distances by use of a piezoelectric positioner. By recording the vertical motion of the pipette as it follows the sample surface, one can generate a topographic image. A current image can also be obtained by direct measurements of the ion current. Three common methods of feedback modes have been developed for SICM: the nonmodulated (dc), distance-modulated (ac), and hopping modes (**Figure 2**).

## 2.1. Nonmodulated Mode

In dc feedback mode (**Figure 2a**), a constant potential difference is applied between electrodes in the pipette and in the bath. The current-distance response for an SICM pipette approaching to a flat surface is illustrated by an approach curve (**Figure 2d**) in which  $d/r_i$  represents the tip-sample distance normalized to the pipette's inner radius. There are two regions in the approach curve: (a) a steady-state region, in which the ion current is unaffected by tip-sample separations and remains close to the maximum current, and (b) another region, in which the ion current declines rapidly as the tip-sample distance decreases. In this region near the surface, the ion current is strongly affected by the pipette position, which provides a method of feedback and control of the pipette in the  $z$  dimension. For samples with high-aspect ratio features, image collection performed very near a sample surface can prove difficult in the dc mode. Tip-sample distances on the order of the inner radius of the pipette have been proposed to prevent surface contact. In this case, the distances from the pipette tip center to the nearest abrupt surface features and to the sample surface right under the pipette tip are similar. Consequently, contact from all directions can be minimized (5).

SICM with nonmodulated feedback provides adequate control needed to analyze biological samples. Submicrometer features of cell membrane surfaces and small membrane changes can also be detected by SICM (1, 5, 8, 9). For living cells with rapid height changes of several micrometers,

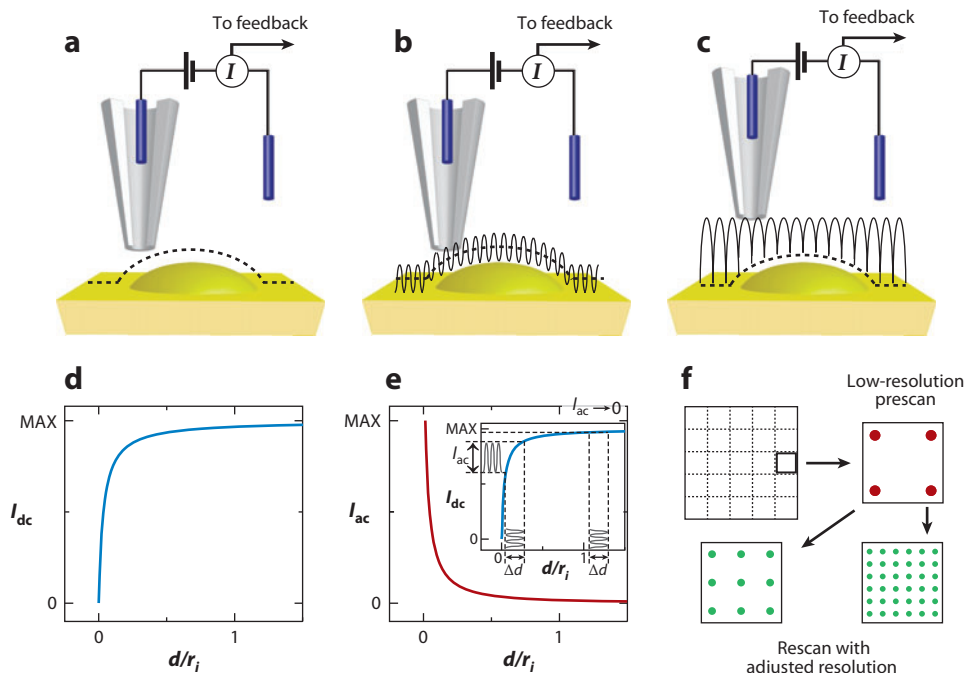


**Figure 2**

(*a–c*) Schematic of nonmodulated (dc), distance-modulated (ac), and hopping feedback modes in scanning ion conductance microscopy. (*a*) Nonmodulated feedback control. In this mode, the dc ion current is sensitive to the tip–surface distance, as shown in (*d*) the dc approach curve, which is used directly to control the position of the pipette.  $d/r_i$  represents the tip–sample distance normalized to the pipette inner radius. (*b*) Distance-modulated feedback control. In this mode, the pipette is modulated with a constant distance ( $\Delta d$ ), which results in a modulated ion current ( $I_{MOD}$ ). In this mode, the ac component of  $I_{MOD}$  is used to maintain the tip–surface distance. Approach characteristics of a modulated pipette are shown in panel *e*, in which  $I_{dc}$  represents the dc component of  $I_{MOD}$ , and  $I_{ac}$  represents the ac component (peak-to-peak amplitude) of  $I_{MOD}$ . (*c*) Hopping feedback control. In this mode, the pipette approaches the sample and withdraws before touching the surface at each imaging point. A prescan is performed with a small number of imaging points to estimate surface roughness, as shown in panel *f*. Thus, rescanning with adjusted resolution can be conducted for different areas as required. Panels *a*, *b*, *d*, and *e* adapted from Reference 6 with permission. Copyright 2001, the Biophysical Society. Panels *c* and *f* adapted from Reference 3 with permission. Copyright 2009, Nature America.

however, the response of dc feedback can be too slow and is susceptible to changes in the ion current that result from dc drift, partial blockage of the pipette, or changes in the ionic strength of the solution. To overcome all these problems, a more reliable feedback control, distance-modulated (ac) mode, was introduced (6).

## 2.2. Distance-Modulated Mode

The ac feedback mode was developed to improve pipette control (6, 10). In this feedback mechanism (**Figure 2b**), the pipette position is modulated vertically at a fixed displacement. As the probe tip approaches the vicinity of the sample surface with pipette modulation, an oscillation in the access resistance is produced; this oscillation introduces an ac component to the preexisting dc current of the pipette to generate a modulated ion current. A lock-in amplifier recovers the

modulated current to be used as a feedback control signal. **Figure 2e** shows the approach curve for the ac feedback mode, which is obtained by plotting the ac component (peak-to-peak amplitude) of the modulated current as a function of normalized tip-sample distances ( $d/r_i$ ). The inset in **Figure 2e** shows the approach curve for the dc component of the modulated current and illustrates how the amplitude of the modulated current changes with tip-sample distance. In the case of nonmodulated feedback, a maximum current is observed when the pipette is located away from the sample, and the current magnitude decreases as the pipette approaches the sample. However, in the case of the modulated current, a signal is observed only when the pipette is very close to the sample.

The surface sensitivity of the modulated current in comparison to the nonmodulated pipette current presents significant advantages with respect to the feedback loop. Modulated feedback is advantageous because changes in the ion current that are not in phase with the modulation frequency do not affect control of the pipette position. With the increased stability of modulated feedback, both long-term, continuous observation of living cells (11, 12) and the ability to maintain control during changes in the ionic strength of the bath solution have been realized (6, 11, 12).

### 2.3. Backstep, Hopping, and Standing Approach Modes

The backstep (2, 13), hopping (3), and standing approach (4) modes of imaging were developed for samples with highly complex surface features. These feedback modes employ a series of approach curves to determine sample topography.

In these modes, the pipette approaches a surface to a defined distance, is withdrawn and repositioned, and then approaches the surface again at the new location (**Figure 2c**). The number of imaging points determines both resolution and imaging time. In hopping mode, to speed up image collection, the surface is imaged first at low resolution to determine sample complexity and estimate roughness (**Figure 2f**). High-resolution imaging can thus be conducted in areas with more complex structures. Regions that are less interesting can be imaged with fewer points, and the distance of pipette withdrawal can also be adjusted to accelerate image collection according to sample roughness. The hopping mode has been used to image challenging samples, namely neurons, which have complex three-dimensional structures. Images obtained with the hopping mode have revealed nanoscale structures in the network formed by axons and dendrites; there was no sample damage from the probe, which demonstrates the ability of this mode to image samples with extremely convoluted surfaces (3).

### 2.4. Scanning Ion Conductance Microscopy Probes

Various geometrical and unique fluidic properties of scanned nanopipettes are of primary importance to the operation and development of SICM. In this section, we briefly discuss the fabrication and characterization of nanopipettes commonly utilized in SICM and give some examples of their applications.

**2.4.1. Single-barrel nanopipettes.** SICM employs a nanopipette (14), which can be easily fabricated, as the scanning probe. To prepare a nanopipette, a clamped capillary is softened by a heat source (filament, flame, or laser), and a mechanical pull separates the capillary to form a pair of pipettes. Through the adjustment of puller parameters, pipettes with different cone angles, taper lengths, and tip diameters can be obtained. **Figure 1b** shows a borosilicate nanopipette fabricated by a CO<sub>2</sub> laser-based puller with a nominal inner diameter of 60 nm. Quartz capillaries have been used to prepare small tips with reported diameters of ~8 nm (4).

**2.4.2.  $\Theta$  nanopipettes.** In addition to single-barrel nanopipettes,  $\Theta$  nanopipettes have also been utilized extensively in SICM applications (15, 16). Such nanopipettes are pulled from  $\Theta$  capillaries to form pipettes such as that shown in **Figure 1c**. Each barrel can be filled with different electrolyte solutions; electrical control of each individual barrel can be achieved when independent electrodes are placed inside of each barrel. These nanopipettes are used to deposit species onto a sample by voltage pulsing (15, 16). Capillaries with more than two barrels are also available; they potentially allow more reagents to be delivered independently from the same pipette.

**2.4.3. Special considerations of the fluidics of nanopipettes.** The small scale and tapered geometry of nanopipettes give rise to several interesting fluidic phenomena that can be important in SICM. Rectification of the ion current is often observed in nanoscale pipettes, in particular when the pipette tip size becomes comparable to the thickness of the electrical double layer. The exact origins of rectification across all sizes of nanopore openings are still under debate. Surface conductance and conductance states for charged species within pipettes are reported to be important factors (17, 18). A charged surface, such as dissociated silanol groups on a glass surface or from chemical modifications of pipette walls, is required for rectified current flow. A recent report employed rectification exhibited by nanopipettes brought in close proximity to a surface as a transducer of surface charge (19).

Due to the tapered geometry of a nanopipette, a potential difference (hundreds of millivolts) applied between the electrode in the nanopipette and in the bath can result in a high electric field (kilovolts per centimeter) localized at the tip (20). This focused electric field makes SICM probes especially sensitive to conductivity changes at the tip, as opposed to the entire nanopipette structure (14). Depending on the applied potential, electrophoresis, electroosmosis, and dielectrophoresis may contribute to the net flow of ions. In cases in which highly conductive electrolyte is involved, the electroosmotic flow arising from the electrical movement of counterions of pipette surface charge is small and negligible. Interestingly, under proper conditions, dielectrophoretic and electrophoretic forces can balance at the pipette tip to induce dielectrophoretic trapping of proteins, nucleic acids, and small molecules (21, 22).

When combined with SICM, dielectrophoretic trapping can be exploited for the controlled delivery of material from the tip of the SICM probe. In this technique, SICM is utilized to control the position of delivery. Dielectrophoresis or electrophoresis can be utilized to concentrate molecules and to control deposition through the potential waveform that is applied (23). Delivery of acid or base through an SICM probe can cause localized pH changes within a few micrometers; a steady-state pH can be maintained from 10 ms to more than 10 min with high dosing concentrations (24). Delivery of fluorescent probe molecules from a nanopipette to different positions at the membranes of sperm cells demonstrated the existence of diffusion barriers and different subregions of the cell membrane (25). When a functionalized substrate is used, deposition of reactive species can generate surfaces with submicrometer patterns. Patterned surfaces have also demonstrated that after voltage deposition from the pipette, biological molecules retain activity; specifically, antibodies are still capable of specific recognition, and DNA can hybridize with complementary strands (26).

## 2.5. Resolution and Theoretical Models

Resolution in SICM is determined by the pipette tip geometry and tip-sample distance, and the typical resolution for SICM is  $\sim 10$  nm vertically and  $\sim 50$  nm laterally (27). The highest resolution reported is 3–6 nm, which was achieved by imaging S-layer proteins from *Bacillus sphaericus* on a mica surface with a nanopipette whose tip was estimated to be 13 nm in inner diameter (28).

SICM resolution has also been examined with simulations in which lateral resolution is defined as the smallest distance between two particles at which individual particles can be resolved in an image. The resolution determined was approximately three times the size of the inner radius of the pipette tip (29). More examples with details are discussed in Sections 3–6, below.

Several models for SICM have been proposed to describe how ion current changes as a function of pipette geometry and surface topography as well as how tip-sample distances affect image resolution and lead to possible image artifacts (7, 29–31). For single-barrel nanopipettes, finite element models predict that ion current drops at larger tip-sample distances for pipettes with a larger tip diameter, a greater cone angle, or a higher ratio of outer radius to inner radius. In addition to flat surfaces, a cylindrical pit, a step, and particles of different heights have been included in these models to study the current characteristics of a pipette as it interacts with different sample structures. In scans of structures with instantaneous steps, image artifacts have been found, which can be explained by the different ion pathways that may occur when the pipette scans over a step (31). The models also predict that nonuniform electric fields at the pipette tip can lead to artifacts (29). Overall, simulations have improved our understanding of the basic concepts of SICM and may help guide future experiments.

---

**AFM:** atomic force microscopy

**SECM:** scanning electrochemical microscopy

---

### 3. ATTRIBUTES OF SCANNING ION CONDUCTANCE MICROSCOPY

The primary advantages of SICM include noncontact surface imaging and the ability to image with inert (e.g., not electrochemically or photonically active) ions, as discussed in the following sections.

#### 3.1. Noncontact Surface Imaging

Atomic force microscopy (AFM) is a good comparator for SICM: AFM can image with high resolution. However, AFM is a force-based technique, and nonzero forces are typically encountered during imaging, even in tapping mode. These forces increase the probability of damage to or deformation of soft and fragile features (32–34). In contrast, SICM can perform noncontact imaging of fragile (35) or highly convoluted surface features (3, 5).

**Figure 3** directly compares SICM and AFM in terms of the imaging of delicate features; alternating sequences of SICM and AFM images for small and loosely attached cellular extensions of a fixed fibroblast cell have been recorded. Images of fibroblast extensions obtained with AFM present obvious morphological distortions that result from the inherent imaging force, whereas no evident topographic deformation has been observed in SICM images (34). Even though SICM is noncontact, the motions of the probe in close proximity to sample surfaces, or distortions of the local electric field from the pipette tip, can generate interactions with the specimen under study. Such noncontact interaction has been exploited in directing the growth of neurons, as described in Section 5 (36, 37).

#### 3.2. Inert Imaging Mediators

Scanning electrochemical microscopy (SECM) is another powerful scanning probe technique for the study of electrochemical properties in versatile biophysical systems (38). The feedback signal utilized in SECM is typically generated via electron-transfer reactions of redox mediators at the probe tip. Consequently, the capability of SECM for the investigation of live biological specimens may be limited if the redox mediator interferes with the sample in some way (e.g., toxicity) or if the electrical properties of the tip are fouled during operation in biological media (39, 40). The



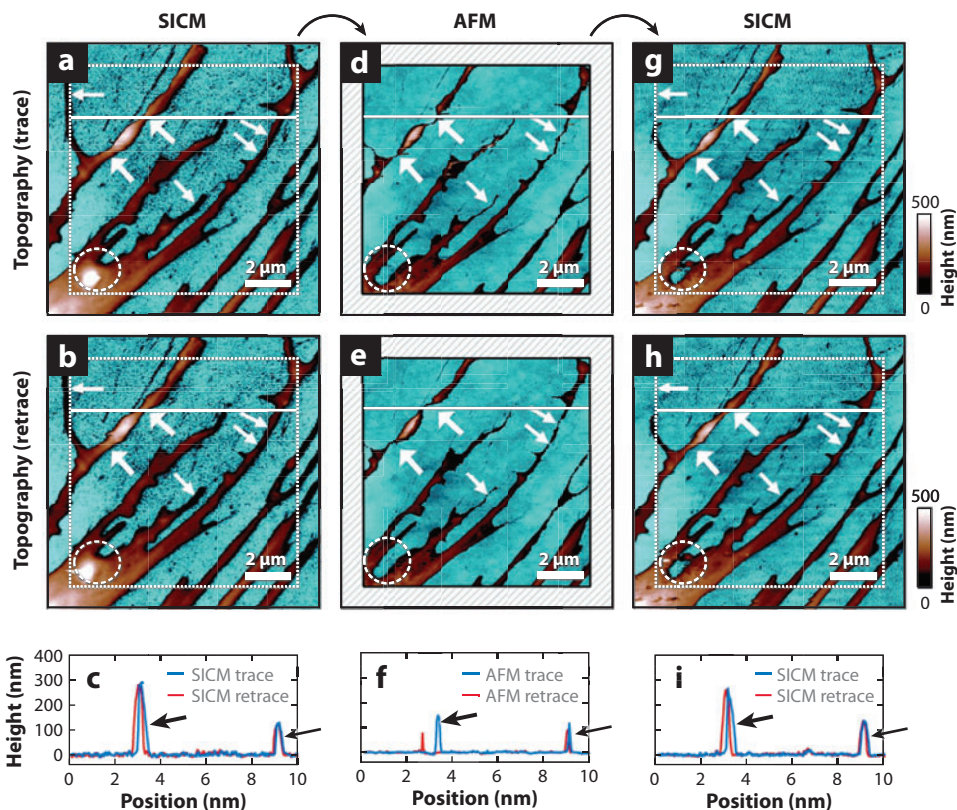


**Figure 3**

Successive SICM-AFM-SICM image sequence. (*a,b*) Fibroblast extensions were imaged by using scanning ion conductance microscopy (SICM) first to obtain (*a*) the trace image (in which the probe moves from left to right) and (*b*) the simultaneously recorded retrace image (in which the probe moves from right to left). (*c*) Respective height profiles along the horizontal lines in panels *a* and *b*. (*d,e*) Weakly attached sections are shifted laterally by the atomic force microscopy (AFM) tip (*thick arrows*). These observations are also apparent in (*f*) the respective height profiles. (*g,h*) SICM images and (*i*) height profiles recorded after the AFM images. The weakly attached sections appear stable again (*thick arrows*); however, one extension (*dashed circle*) may have been permanently damaged by AFM imaging. Reprinted with permission from Reference 34. Copyright 2010, American Chemical Society.

same drawback, namely signal transduction that interferes with sample function, may also arise in the case of fluorescence microscopy, in which fluorescent dyes or fluorescently tagged proteins can alter the properties of the system under study.

SICM can correlate topographic information with transport properties of electrochemically inactive ions, such as  $K^+$  and  $Cl^-$ , by conductance measurements. The electrolyte concentrations employed in SICM can be commensurate with conditions for cell viability, so limited extra steps or additives are required. Variations in ion concentrations at small scales have been measured with SICM, which is difficult to achieve otherwise. In the vicinity of nanopores on polymer membranes, local variations in conductance, which are generated from concentration gradients across the membrane, have been mapped with SICM. The ability to discern ion-transport pathways from porous materials with heterogeneous surface features has also been demonstrated (41, 42).



## 4. LIVE-CELL IMAGING

With advances in position-control systems and the fabrication of nanosized scanning probes, SICM has been employed to image living cells with rough surfaces and branching processes (5, 8). Recently, long-term, real-time, and high-resolution investigations of complex specimens with SICM have proven possible. SICM has become a powerful technique for biological investigations, such as morphological characterization, assessment of physiological activity, and dynamic observations of subcellular structures.

### 4.1. Characterization of Cellular Morphology

SICM's noninvasive nature and ability to operate in physiological buffers make it a suitable method for investigation of cellular morphology. To determine the capability of SICM for characterization of morphological features of living cells, investigators examined the reproducibility of the scans. For the line-scan mode, the standard deviation at the plateau of the cell body of five repeated lines was determined to be 50 nm, whereas the standard deviation was up to 700 nm at the border of the cell, where changes in cell height are steep (13). In addition, raster scans generated a three-dimensional map of the apical cell surface, which provides information associated with cell size and cell height and, thus, makes whole-cell volume measurements possible. In other studies, a wide range of volumes (from  $10^{-4}$  to  $10^6 \mu\text{m}^3$ ) were measured, and the spatial resolution for cell volume measurements was reported to be  $2.5 \times 10^{-5} \mu\text{m}^3$  with an error of only 0.2%. Cell surface and cell roughness were also examined quantitatively and had resolutions of up to  $4.5 \times 10^{-3} \mu\text{m}^2$  and  $10^{-2} \mu\text{m}$ , respectively (43).

In 2009, further advances in the feedback control system improved the resolution of SICM to the nanometer scale. With hopping mode methodology, SICM can supplement interpretations of single-particle tracking for membrane dynamics studies (44). This technique can also resolve the most convoluted and delicate structures, such as auditory hair cells and synaptic boutons or axons of neural cells (3, 4). In addition, subpopulations of cell lines with cellular heterogeneity, in which several phenotypic variants exist simultaneously and can transdifferentiate to other cell types, can be distinguished from one another. SK-N-SH cells, a model of neuroblastoma (the most common pediatric extracranial solid cancer), which contains three different phenotypic variants with distinct morphological attributes, were examined with hopping mode ICM. In addition to cell shape, spread range, cell height, and cell volume, fine membrane structures—such as cell roughness and types of membrane protrusions—can be investigated in detail. There are numerous applications for this capability, notably pathology studies of tumor cells (45).

### 4.2. Real-Time Imaging of Cellular Activities

Real-time and long-term recordings of continuous changes in morphology have also been investigated with SICM (6). For instance, migration, which involves changes in cell shape, can be explored by examining the images obtained from two consecutive scans. Both the direction of cell movement and changes in cell volume were examined. With this method, investigators showed that immature oligodendrocytes migrate easily and have weak fixation to a poly-L-lysine-coated substrate (13). The migration velocities of mature (differentiated) and immature oligodendrocytes were quantitatively determined to be  $0.86$  and  $4.29 \mu\text{m h}^{-1}$ , respectively; these findings further confirm expectations that differentiated cells are less mobile than immature cells (13, 46).

Cellular activities at different stages of the cell cycle are also of great interest. For instance, the amount of time required for an entire cell cycle differs from organism to organism, requiring

as little as 20 min in bacteria (47) or as much as 24 h in more rapidly dividing mammalian cells (48). Techniques that can provide continuous high-resolution observation of cell cycles are beneficial for the assessment of time-dependent morphological structures associated with many physiological processes. SICM has been employed to investigate changes in the height, volume, and shape of *Xenopus* kidney epithelial cells (A6 cell line) under normal physiological conditions (11). In addition, the processes of cell division and dead cell removal in a confluent A6 epithelial cell monolayer have been demonstrated to take approximately 4 h (12).

### 4.3. Dynamic Investigation of Subcellular Structures

Changes in cellular morphology due to physiological, pharmacological, or molecular stimuli are often accompanied by complex reorganization of subcellular structures. Investigation into these subcellular features, especially for those with nanometer-scale dimensions, presents technical challenges to many conventional imaging techniques. SICM, with its high spatial resolution that can visualize protein complexes with a diameter of approximately 14 nm on the surfaces of living spermatozoa (28), has proven to provide adequate temporal resolution for subcellular dynamic studies (49, 50).

Gorelik et al. (49) reported that SICM can examine the dynamics of microvilli in detail. Microvilli are membrane protrusions supported by a central core that is composed of a dense bundle of cross-linked actin filaments (50). Short, nonspecialized microvilli on the surfaces of most cells, such as epithelial cells and fibroblasts, undergo a three-stage life cycle of approximately 12 min (49). This life cycle starts with a fast, height-dependent growth at an initial rate of approximately  $5 \text{ nm s}^{-1}$ , followed by a steady state and, finally, a slow, height-independent retraction state with a constant rate of approximately  $1.2 \text{ nm s}^{-1}$  (**Figure 4**). Similar microvillus dynamics have been observed in various cell types, including A6 cells, human colon cancer cells, and the epithelial cells of the mouse organ of Corti, demonstrating that these observations are not unique to a certain cell line but rather are widespread cellular phenomena (49).

## 5. MULTIFUNCTIONAL SCANNING ION CONDUCTANCE MICROSCOPY FOR PHYSIOLOGICAL STUDIES

In addition to high-resolution observation of surface topography, SICM can perform multifunctional analysis of living cells. Morphological transformations induced by physiological stimuli, identification of intracellular signaling pathways, and characterization of mechanical responses exemplify the versatility of SICM.

### 5.1. Correlations Between Cellular Morphology and Physiology

SICM exhibits spatial resolution that ranges from whole-tissue to subcellular dimensions, and it has successfully performed multiperspective analysis. For example, SICM can distinguish tissues between the inner and outer parts of the thoracic aorta on the basis of differences in cell shape and arrangement. Shear stress from blood flow is a major contributor to the vascular endothelial cell phenotype (51). Endothelial cells exposed to low and reversing shear stress in the atheroprone region of the aorta, where atherosclerosis tends to occur, were observed by SICM as disordered with a cobblestone appearance. However, cells from the outer part of the thoracic aorta in the atheroprotected region, where the shear stress is relatively high and unidirectional, exhibited an elongated appearance and were aligned in the direction of blood flow (52).

SICM also can identify abnormal topographical changes in cardiomyocytes associated with heart failure. Mature ventricular myocytes are composed of highly organized myofibrils and have

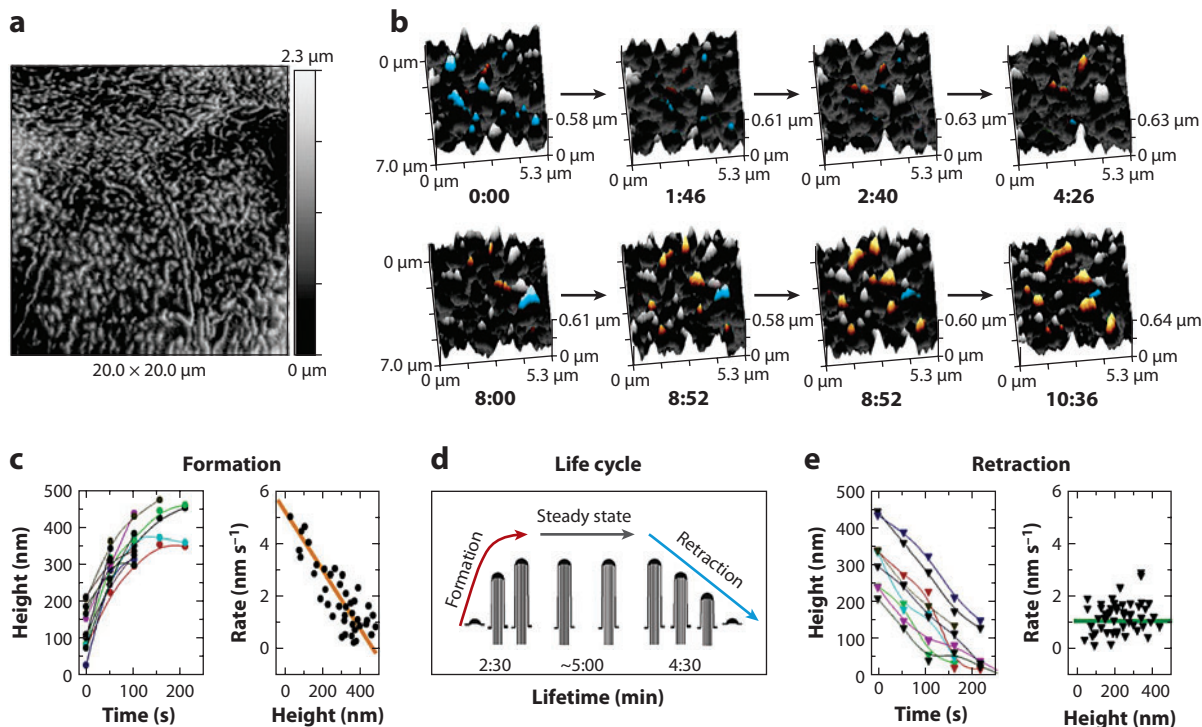


**Figure 4**

Dynamics of individual microvilli in a living epithelial cell (A6 cell line). (a) Topographical scanning ion conductance microscopy image of cells with well-formed microvilli. (b) High-resolution time-lapse imaging of microvilli. Microvilli that are forming, retracting, and relatively stable are highlighted in orange, blue, and white, respectively. (c) (Left) Heights of individual microvilli increase nonlinearly during their formation. (Right) The height-dependent rate of microvilli formation ( $n = 66$ ). (d) Schematic diagram of the life cycle of microvilli: formation, steady state, and retraction. (e) (Left) Individual microvilli undergo a linear decrease of height during retraction. (Right) Height-independent rate of microvilli retraction ( $n = 59$ ). Reprinted with permission from Reference 49. Copyright 2003, National Academy of Sciences.

a domed-crest surface with pronounced, grooved structures ( $z$  grooves). Transverse (T) tubules, which act as major sites for myocyte excitation-contraction coupling, are deep invaginations of the sarcolemma (the plasma membrane of myocytes) and contain a large number of L-type  $\text{Ca}^{2+}$  channels. Ventricular myocytes derived from failing hearts (53), affected by prolonged mechanical unloading (54) or undergoing detubulation induced by osmotic shock or prolonged culture (55), were examined with SICM. In all of these cases, the SICM images revealed obvious changes in the surface structure compared with that of healthy myocytes, including loss of T tubules, flattening of  $z$  grooves, and disruptions in T tubule openings. Along with these distinct changes in cell structures, the normal synchronicity of  $\text{Ca}^{2+}$  release was disrupted, which resulted in slow  $\text{Ca}^{2+}$  transients as well as a diminished and prolonged cardiac contraction (53–56).

## 5.2. Stimulus-Induced Morphological Transformations

The maintenance of constant cell volume is a fundamental cellular homeostatic mechanism. Many living cells can respond to internal or external stimulation by inducing various regulatory reactions

that reorganize cell shape and volume. SICM has been used to monitor the process of regulation of cell volume generated by hypertonic or hypotonic stress (43).

When exposed to a hypertonic solution, hepatic cells undergo a process termed regulatory cell volume increase, in which an initial shrinkage in cell size is followed by a recovery in cell volume to approximately 90% of the original size (46). A contrary mechanism named regulatory cell volume decrease was also examined with SICM. Following transfer from hypertonic solutions to isotonic solutions, hepatic cells exhibited reactive swelling, followed by downregulation of the cell volume to approximately 110% of the original size (46). Additionally, SICM was utilized to assess mechanisms that cultured epithelial cell monolayers utilize to maintain integrity when subjected to apical hyperosmotic stress. Several balloon-like structures (12) were located at the joints of cell junctions. These structures emerged within 20 min of exposure to hypertonic solutions and disappeared after the regulatory cell volume increase procedure and cell membrane recovery occurred. These balloon-like structures may help prevent loss of cell-cell contacts and may retain monolayer permeability when the confluent epithelial cells experience shrinkage in cell volume under hypertonic stress (12).

In addition to osmotic stimulation, changes in cell shape and membrane topography that arise from other molecular or pharmaceutical stimulation were investigated with SICM in diverse cell types (43, 57). For instance, SICM operated in the distance-modulated mode was used to monitor contractions of cardiomyocytes induced by additional extracellular  $\text{Ca}^{2+}$  ions; the resultant cell motions lasted approximately 200 ms in the vertical direction up to 4  $\mu\text{m}$  (6). The protective effects of esmolol from the arrhythmogenic reaction of cardiomyocytes were examined with SICM through the measurement of the vertical displacement and the frequency of cell contractions (58). Furthermore, punctate depressions on the membrane surface of bovine chromaffin cells, generated by high  $\text{K}^+$  stimulation, were observed with SICM and correlated to the exocytosis-induced membrane depolarization of chromaffin cells in a high- $\text{K}^+$  solution in the presence of extracellular  $\text{Ca}^{2+}$  ions (59).

### 5.3. Location of Ion Channels and Membrane Receptors

Evidence suggests that many ion channels, receptors, and transporters are heterogeneously located on the plasma membrane (60, 61). Unique spatial distributions of these membrane components help establish regional specialization within a cell, which results in localized control over cell functions. Evidence related to the distribution of functional membrane components (e.g., ion channels and receptors) has been found with SICM.

In cardiac myocytes, the locations of distinct types of ion channels were mapped with SICM coupled to voltage-clamp techniques. For example, the distribution of ATP-sensitive  $\text{K}^+$  channels ( $\text{K}_{\text{ATP}}$ ) was visualized with ion-channel current recordings, which are obtained with a whole-cell voltage clamp coupled to local stimulus delivery by SICM (Figure 5) (62). Successive current images recorded over a relatively long period of observation (longer than 40 min) revealed that  $\text{K}_{\text{ATP}}$  channels have low lateral mobility and concentrate in localized regions along the  $z$  grooves of the sarcolemma (62). Further, the excitation-contraction coupling of cardiac myocytes was regulated by voltage-dependent L-type  $\text{Ca}^{2+}$  channels via  $\text{Ca}^{2+}$ -induced  $\text{Ca}^{2+}$  release. In this process, extracellular  $\text{Ca}^{2+}$  enters myocytes through open L-type  $\text{Ca}^{2+}$  channels and triggers  $\text{Ca}^{2+}$  release from intracellular stores (63). To locate L-type  $\text{Ca}^{2+}$  channels, the SICM probe was adapted to a patch-clamp pipette utilized to record cell-attached  $\text{Ba}^{2+}$  currents through the  $\text{Ca}^{2+}$  channels at different regions of the cardiomyocyte sarcolemma, including T tubule openings,  $z$  grooves, and domed crests. The recorded electrophysiological measurements revealed that the

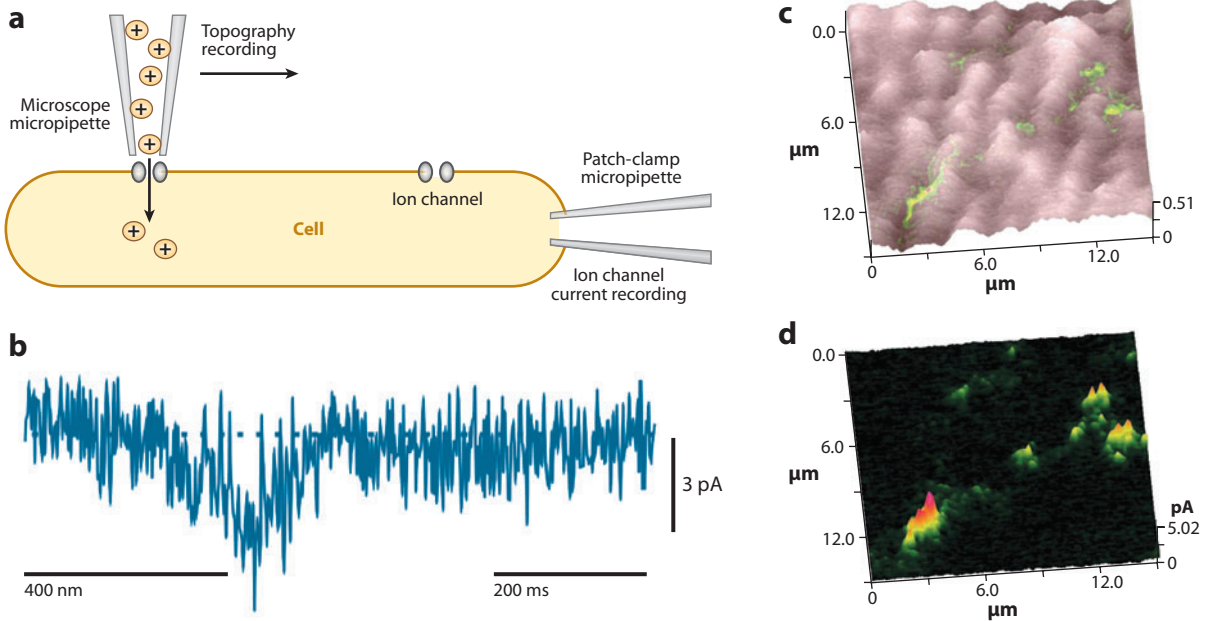


**Figure 5**

(a) Diagram of the sensing mechanism of the combined scanning ion conductance microscopy (SICM)/whole-cell voltage-clamp technique for functional localization of single ion channels in intact cell membranes. (b) A single-channel current record obtained from a line scan of the nanopipette over the cell surface, which allows for detection of a single  $K_{ATP}$  channel position in rat cardiomyocyte sarcolemma. (c) Combined SICM topographic image of a cardiomyocyte and a map of the  $K^+$  current, showing that the  $K_{ATP}$  channels occur in the parallel grooves ( $z$  grooves) of the sarcolemma. (d) The same imaging area as in panel c, showing only the ion-channel activity. Note that activity varies between different clusters of ion channels. Reproduced with permission from Reference 62. Copyright 2000, *Nature*.

distribution of L-type  $Ca^{2+}$  channels was concentrated in the membrane of the T tubule system (52).

For membrane-associated receptors, purinergic (P2) receptors, which regulate amiloride-sensitive epithelial sodium channels, were found at both the basolateral and apical membranes of epithelia (64–66). Apical P2 receptors inhibit  $Na^+$  transport in the presence of extracellular ATP (67, 68). Cell morphological responses recorded with SICM, coupled with transepithelial electrical resistance measurements, showed that ionotropic  $P2X_4$ -like receptors were located at the basolateral membrane of A6 cells and facilitated  $Na^+$  transport across the epithelia (69, 70). SICM coupled to fluorescence resonance energy transfer (FRET) microscopy was employed to investigate the spatial localization of  $\beta_1$ - and  $\beta_2$ -adrenergic receptors ( $\beta$ ARs) found on the surface of cardiomyocytes. Use of the SICM/FRET technique showed that  $\beta_2$ ARs were located exclusively in the T tubule region of cardiomyocytes derived from healthy adult rats, whereas  $\beta_1$ ARs were evenly distributed over the entire sarcolemma. Additionally, for cells isolated from rats with chronic heart failure,  $\beta_2$ ARs were redistributed from the T tubule system to the domed-crest region of cardiomyocytes; this redistribution altered the signaling compartmentalization of cyclic AMP and, therefore, its physiological function (52, 71).



**SNOM:** scanning near-field optical microscopy

**SSCM:** scanning surface confocal microscopy

## 5.4. Mechanical Responses of Living Cells

Living cells can sense and respond to mechanical stress from both external environmental conditions and internal physiological conditions. Understanding the cellular response to physical stimulations is important for the determination of how cells transmit and convert mechanical stress into biochemical or physiological responses. SICM has been used to investigate the mechanical responses of living cells, such as the effect of chronic heterogeneous shear stress on endothelial cell morphology (72) and the stiffness of the plasma membrane under applied hydrostatic pressure (73).

When employed in imaging the neural cells of a leech, SICM induced consistent perturbation of neuronal growth cones through an interaction between the scanning probe and the sample. Such probe-sample interaction was characterized as a weak hydrostatic force (37) due to the level of the pipette filling solution. This interaction persisted even in the far-scanning regime, which is generally regarded as noncontact imaging. Through the use of recurrent line scans along a defined direction, new growth cone processes were induced; this observation demonstrated that although SICM is considered a noncontact imaging technique, the hydrostatic force at the SICM probe can be exploited to remodel neuronal growth cones or to direct neurons in designed networks (36, 37).

## 6. HYBRID TECHNIQUES

Considerable efforts have been made to integrate SICM with conventional optical or electrical measurements. The ability to control the position of the SICM probe with high resolution offers opportunities to “piggyback” on additional analytical signals (i.e., photonic or electrical ones) to increase the amount of chemical information obtained from the measurements. Doing so often requires the fabrication of unique probes for the incorporation of multiple signals.

### 6.1. Coupling with Optical Measurement

To facilitate selection of the sample areas to be imaged, SICMs are usually mounted on an inverted optical microscope equipped with micromanipulators to assist positioning of the scanning frames (74). The use of optics saves considerable time in the coarse positioning and approach process. In addition, the optical images obtained complement the scanning images obtained with SICM.

To increase chemical specificity, scanning near-field optical microscopy (SNOM) (75) and confocal fluorescence microscopy (76–78) have been combined with SICM to allow simultaneous recording of photonic information with SICM images. Cardiac myocytes with pronounced domed-crest features on the sarcolemma demonstrated the capability of the hybrid SICM/SNOM microscope. In this instrument, the SICM probe, which served as the output aperture of SNOM, was back-inserted with an optical fiber and coated with a thin (~100–150 nm) layer of aluminum (75). This setup allowed for reliable control of small probe-surface distances for the SNOM tip with the SICM feedback system. Differences in interactions between the near-field source and the cell surface were represented as changes in the contrast of optical images resolved with SNOM and were correlated with the topographic features recorded with SICM. Through the use of this method, morphological features of rabbit cardiac myocytes, such as *z* grooves, were characterized with SICM (75).

Confocal fluorescence microscopy was integrated with SICM to develop a new technique termed scanning surface confocal microscopy (SSCM) (76). In SSCM, a sample-scanned configuration was utilized for SICM. In sample-scanned SICM, the SICM probe is modulated



perpendicularly to the sample surface, and the sample is imaged by raster scanning of the sample stage instead of the SICM probe; feedback control maintains constant tip-sample distance. Light from the confocal microscope is focused in the volume immediately below the probe tip (76). With this setup, surface confocal fluorescence images and corresponding SICM topographic images can be obtained simultaneously. SSCM has been utilized to study the entry process of virus-like particles into a cell (76, 78) and to identify the endocytic pathways of Cos-7 cells mediated by different proteins such as clathrin, caveolins, and flotillin (77). Through the correlation between changes at the surface of the cell membrane and the presence of fluorescently labeled particles, interactions of specific molecules with target cells can be examined, thereby expanding the application of SICM-based techniques to investigations of the relationship between fluorescently tagged species and cell membrane components.

---

**SECCM:** scanning electrochemical cell microscopy

---

## 6.2. Coupling with Other Methods

Before the development of distance-modulated feedback, which improved the stability of SICM, AFM was combined with SICM to provide feedback control that is independent of ion current measurements. In this combined SICM/AFM technique, deflection of light from the back of a bent pipette was utilized as the feedback signal; the nanopipette served as both a cantilever and a current-sensitive probe (79). With this setup, topographic imaging with the nanopipette can be operated under both the contact and tapping modes of AFM, and ion current images of the scanned surface can be recorded simultaneously. This hybrid technique can resolve the conductive pathways of synthetic polycarbonate membranes with nonhomogeneous surface features (79).

Standard SICM techniques remain insensitive to faradic electrochemical processes. In contrast, SECM can provide spatial mapping of electrochemistry for a wide range of materials, including insulators (80, 81), metals (82, 83), and semiconductors (84, 85). Integration of SECM and SICM was recently achieved through the fabrication of new electrodes. In this SECM/SICM technique, a pipette-based probe with an insulated conductive layer (Au or Pt) coating the outer surface of the pipette tip was utilized. The ion current produced through the hollow geometry of the pipette served as the control signal for the SICM feedback system, and the ring-shaped conductive material exposed at the pipette tip was utilized as a nanoring electrode for electrochemical measurements. With this hybrid technology, topography and the corresponding electrochemical response for single live cells, enzyme spots, and Au film electrodes were successfully resolved at submicrometer resolution (86, 87).

Scanning electrochemical cell microscopy (SECCM), a technique closely related to SICM/SECM, employs two-barrel  $\theta$  pipettes to probe electrochemical dynamics at interfaces. A small meniscus formed at the end of the  $\theta$  pipette tip is scanned along a conductive, biased surface, such as Au strips (88) or carbon nanotubes (89). This  $\theta$  pipette does not require a bath electrolyte to produce an ion current as the feedback signal. The ion current is generated from the electrode in one barrel of the  $\theta$  pipette to the second electrode in the other barrel through the meniscus at the end of the tip. Consequently, the current magnitude is affected by the shape and the volume of the meniscus, which deforms when the meniscus touches the surface under study and therefore provides a method to determine the tip-sample distance. Owing to this unique mechanism for production of the ion current and control of the vertical probe position, only a small portion of the surface under study comes into contact with the solution within a brief period of time. This attribute makes SECCM a promising tool for the study of systems in which surface fouling, corrosion, and passivation are problematic. Hence, SECCM, which provides complementary electrochemical analysis to simultaneous topographic and conductance

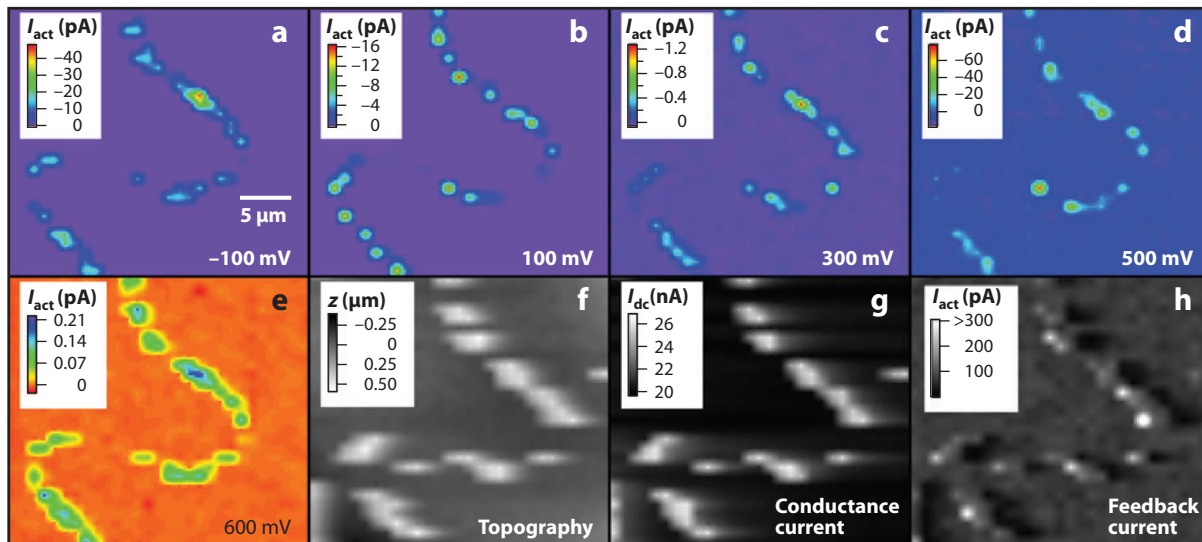


**Figure 6**

Scanning electrochemical cell microscopy (SECCM) images of Pt particles deposited on a carbon nanotube on a  $\text{SiO}_2$  substrate. (a–e) Electrochemical response (currents) at various potentials relative to the Pd- $\text{H}_2$  quasi-reference electrode. Note that the currents at 600 mV are oxidative currents. (f) Apparent surface topography. (g) The dc conductance current between the two barrels of the SECCM probe. (h) The ac component of the conductance current. Panels f–h were recorded at a sample potential of 300 mV. Reprinted with permission from Reference 89. Copyright 2011, American Chemical Society.

measurements (**Figure 6**), becomes a possible platform to investigate gas exchange at the meniscus for studies involved in gas-liquid-solid (electrode) interfaces is promising (89).

### 6.3. Scanning Patch-Clamp Technique

Patch-clamp techniques have had a major impact on the fields of electrophysiology and medicine (90). Measurement of membrane electrical activity with high temporal resolution of various excitable cells, such as cardiomyocytes (91, 92) and neurons (93–95), exemplifies some of the applications of this technique.

The patch-clamp technique, however, lacks adequate spatial resolution for studies related to the localization of ion channels. SICM equipped with a pipette-based probe successfully incorporated patch-clamp recordings, with subcellular resolution, into the topographical images of living cells. This SICM-based patch-clamp method, termed the scanning patch-clamp or “smart” patch-clamp technique (96, 97), can perform electrophysiological recordings by positioning the nanopipette at specific locations predefined from high-resolution topographic SICM images. This technique has been used to study the regional specialization in cells established by unique spatial distribution of ion channels and receptor proteins on the plasma membrane (Section 5.3). In addition to identifying the localization of ion channels for different ions such as  $\text{Ca}^{2+}$  and  $\text{K}^+$ , this technique also recognized the individual distributions of three types of  $\text{Cl}^-$  channels on cardiomyocytes. The scanning patch-clamp technique revealed that these three  $\text{Cl}^-$  channels are located only in the regions of  $z$  grooves and around the opening of T tubules with distinct distribution probabilities (98, 99).

## SUMMARY POINTS

1. Over the past decade, SICM has become a versatile noncontact imaging tool on the basis of advances in feedback control systems and probe fabrication, as well as its ability to integrate with various existing technologies.
2. Development of hopping mode for feedback systems greatly improves the resolution of SICM, which permits the investigation of delicate and highly convoluted subcellular structures.
3. Application of conductive nanopipettes or  $\theta$  pipettes enables SICM to record electrochemical properties that are complementary to topographic and conductance images. Other hybrid SICM techniques, such as the combination of SICM and FRET microscopy, confocal microscopy, and patch-clamp techniques, are further extending the practical applications of SICM into the fields of molecular biology and cellular physiology.
4. SICM is becoming a more mature technology that can achieve noninvasive, high-resolution imaging. It is providing new opportunities for investigation in various physical and biological systems.

## FUTURE ISSUES

1. What new techniques will be incorporated into SICM to extend the information content of the data collected—mass spectrometry? More advanced subdiffraction-limited fluorescence microscopy?
2. Simplification of the operation of SICM to promote more widespread adoption of this technique will extend its applications.
3. Improvements in routine resolution would benefit overall applications, which may depend on better methods to reproducibly prepare ultrasmall pipettes.

## DISCLOSURE STATEMENT

The authors are not aware of any affiliations, memberships, funding, or financial holdings that might be perceived as affecting the objectivity of this review.

## ACKNOWLEDGMENTS

The authors are supported by the National Institutes of Health and the American Heart Association. We acknowledge Ms. Celeste Morris for comments and the electron micrographs in **Figure 1** and Mr. Rahul Thakar for comments on the manuscript. We also acknowledge the authors of the studies reviewed.

## LITERATURE CITED

1. Hansma PK, Drake B, Marti O, Gould SAC, Prater CB. 1989. The scanning ion-conductance microscope. *Science* 243:641–43
2. Mann SA, Hoffmann G, Hengstenberg A, Schuhmann W, Dietzel ID. 2002. Pulse-mode scanning ion conductance microscopy—a method to investigate cultured hippocampal cells. *J. Neurosci. Methods* 116:113–17

3. Novak P, Li C, Shevchuk AI, Stepanyan R, Caldwell M, et al. 2009. Nanoscale live-cell imaging using hopping probe ion conductance microscopy. *Nat. Methods* 6:279–81
4. Takahashi Y, Murakami Y, Nagamine K, Shiku H, Aoyagi S, et al. 2010. Topographic imaging of convoluted surface of live cells by scanning ion conductance microscopy in a standing approach mode. *Phys. Chem. Chem. Phys.* 12:10012–17
5. Korchev YE, Bashford CL, Milovanovic M, Vodyanoy I, Lab MJ. 1997. Scanning ion conductance microscopy of living cells. *Biophys. J.* 73:653–58
6. Shevchuk AI, Gorelik J, Harding SE, Lab MJ, Klenerman D, Korchev YE. 2001. Simultaneous measurement of  $\text{Ca}^{2+}$  and cellular dynamics: combined scanning ion conductance and optical microscopy to study contracting cardiac myocytes. *Biophys. J.* 81:1759–64
7. Nitz H, Kamp J, Fuchs H. 1998. A combined scanning ion-conductance and shear-force microscope. *Probe Microsc.* 1:187–200
8. Korchev YE, Milovanovic M, Bashford CL, Bennett DC, Sviderskaya EV, et al. 1997. Specialized scanning ion-conductance microscope for imaging of living cells. *J. Microsc.* 188:17–23
9. Schraml S. 2003. *Setup and application of a scanning ion conductance microscope*. PhD thesis. Vienna Univ. Technol., Vienna
10. Li C, Johnson N, Ostanin V, Shevchuk A, Ying LM, et al. 2008. High resolution imaging using scanning ion conductance microscopy with improved distance feedback control. *Prog. Nat. Sci.* 18:671–77
11. Gorelik J, Zhang YJ, Shevchuk AI, Frolenkov GI, Sanchez D, et al. 2004. The use of scanning ion conductance microscopy to image A6 cells. *Mol. Cell. Endocrinol.* 217:101–8
12. Zhang YJ, Gorelik J, Sanchez D, Shevchuk A, Lab M, et al. 2005. Scanning ion conductance microscopy reveals how a functional renal epithelial monolayer maintains its integrity. *Kidney Int.* 68:1071–77
13. Happel P, Hoffmann G, Mann SA, Dietzel ID. 2003. Monitoring cell movements and volume changes with pulse-mode scanning ion conductance microscopy. *J. Microsc.* 212:144–51
14. Morris CA, Friedman AK, Baker LA. 2010. Applications of nanopipettes in the analytical sciences. *Analyst* 135:2190–202
15. Rodolfa KT, Bruckbauer A, Zhou DJ, Korchev YE, Klenerman D. 2005. Two-component graded deposition of biomolecules with a double-barreled nanopipette. *Angew. Chem. Int. Ed.* 44:6854–59
16. Rodolfa KT, Bruckbauer A, Zhou DJ, Shevchuk AI, Korchev YE, Klenerman D. 2006. Nanoscale pipetting for controlled chemistry in small arrayed water droplets using a double-barrel pipet. *Nano Lett.* 6:252–57
17. Woermann D. 2003. Electrochemical transport properties of a cone-shaped nanopore: high and low electrical conductivity states depending on the sign of an applied electrical potential difference. *Phys. Chem. Chem. Phys.* 5:1853–58
18. Siwy ZS. 2006. Ion-current rectification in nanopores and nanotubes with broken symmetry. *Adv. Funct. Mater.* 16:735–46
19. Sa N, Baker LA. 2011. Rectification of nanopores at surfaces. *J. Am. Chem. Soc.* 133:10398–401
20. Ying LM, White SS, Bruckbauer A, Meadows L, Korchev YE, Klenerman D. 2004. Frequency and voltage dependence of the dielectrophoretic trapping of short lengths of DNA and dCTP in a nanopipette. *Biophys. J.* 86:1018–27
21. Clarke RW, White SS, Zhou DJ, Ying LM, Klenerman D. 2005. Trapping of proteins under physiological conditions in a nanopipette. *Angew. Chem. Int. Ed.* 44:3747–50
22. Piper JD, Clarke RW, Korchev YE, Ying LM, Klenerman D. 2006. A renewable nanosensor based on a glass nanopipette. *J. Am. Chem. Soc.* 128:16462–63
23. Ying LM, Bruckbauer A, Rothery AM, Korchev YE, Klenerman D. 2002. Programmable delivery of DNA through a nanopipet. *Anal. Chem.* 74:1380–85
24. Piper JD, Li C, Lo CJ, Berry R, Korchev Y, et al. 2008. Characterization and application of controllable local chemical changes produced by reagent delivery from a nanopipet. *J. Am. Chem. Soc.* 130:10386–93
25. Bruckbauer A, James P, Zhou DJ, Yoon JW, Excell D, et al. 2007. Nanopipette delivery of individual molecules to cellular compartments for single-molecule fluorescence tracking. *Biophys. J.* 93:3120–31
26. Bruckbauer A, Zhou DJ, Ying LM, Korchev YE, Abell C, Klenerman D. 2003. Multicomponent submicron features of biomolecules created by voltage-controlled deposition from a nanopipet. *J. Am. Chem. Soc.* 125:9834–39

27. Ying LM, Bruckbauer A, Zhou D, Gorelik J, Shevchuk A, et al. 2005. The scanned nanopipette: a new tool for high-resolution bioimaging and controlled deposition of biomolecules. *Phys. Chem. Chem. Phys.* 7:2859–66
28. Shevchuk AI, Frolenkov GI, Sanchez D, James PS, Freedman N, et al. 2006. Imaging proteins in membranes of living cells by high-resolution scanning ion conductance microscopy. *Angew. Chem. Int. Ed.* 45:2212–16
29. Rheinländer J, Schaffer TE. 2009. Image formation, resolution, and height measurement in scanning ion conductance microscopy. *J. Appl. Phys.* 105:094905
30. Adenle O, Fitzgerald W. 2005. Simulating imaging with the scanning ion-conductance microscope. *Conf. Proc. IEEE Eng. Med. Biol. Soc.* 4:3410–13
31. Edwards MA, Williams CG, Whitworth AL, Unwin PR. 2009. Scanning ion conductance microscopy: a model for experimentally realistic conditions and image interpretation. *Anal. Chem.* 81:4482–92
32. Jiao Y, Schaffer TE. 2004. Accurate height and volume measurements on soft samples with the atomic force microscope. *Langmuir* 20:10038–45
33. Hennesthal C, Drexler J, Steinem C. 2002. Membrane-suspended nanocompartments based on ordered pores in alumina. *ChemPhysChem* 3:885–89
34. Rheinländer J, Geisse NA, Proksch R, Schäffer TE. 2010. Comparison of scanning ion conductance microscopy with atomic force microscopy for cell imaging. *Langmuir* 27:697–704
35. Böcker M, Muschter S, Schmitt EK, Steinem C, Schäffer TE. 2009. Imaging and patterning of pore-suspending membranes with scanning ion conductance microscopy. *Langmuir* 25:3022–28
36. Pellegrino M, Orsini P, De Gregorio F. 2009. Use of scanning ion conductance microscopy to guide and redirect neuronal growth cones. *Neurosci. Res.* 64:290–96
37. Pellegrino M, Orsini P, Pellegrini M, Baschieri P, Dinelli F, et al. 2011. Weak hydrostatic forces in far-scanning ion conductance microscopy used to guide neuronal growth cones. *Neurosci. Res.* 69:234–40
38. Amemiya S, Bard AJ, Fan FRF, Mirkin MV, Unwin PR. 2008. Scanning electrochemical microscopy. *Annu. Rev. Anal. Chem.* 1:95–131
39. Black M, Cooper J, McGinn P. 2004. Scanning electrochemical microscope characterization of thin film Pt-Ru alloys for fuel cell applications. *Chem. Eng. Sci.* 59:4839–45
40. Zoski CG, Simjee N, Guenat O, Koudelka-Hep M. 2004. Addressable microelectrode arrays: characterization by imaging with scanning electrochemical microscopy. *Anal. Chem.* 76:62–72
41. Chen C-C, Derylo MA, Baker LA. 2009. Measurement of ion currents through porous membranes with scanning ion conductance microscopy. *Anal. Chem.* 81:4742–51
42. Chen C-C, Baker LA. 2011. Effects of pipette modulation and imaging distances on ion currents measured with scanning ion conductance microscopy (SICM). *Analyst* 136:90–97
43. Korchev YE, Gorelik J, Lab MJ, Sviderskaya EV, Johnston CL, et al. 2000. Cell volume measurement using scanning ion conductance microscopy. *Biophys. J.* 78: 451–57
44. Adler J, Shevchuk AI, Novak P, Korchev YE, Parmryd I. 2010. Plasma membrane topography and interpretation of single-particle tracks. *Nat. Methods* 7:170–71
45. Liu X, Yang X, Zhang B, Zhang XF, Lu HJ, et al. 2011. High-resolution morphological identification and characterisation of living neuroblastoma SK-N-SH cells by hopping probe ion conductance microscopy. *Brain Res.* 1386:35–40
46. Happel P, Wehner F, Dietzel ID. 2007. Scanning ion conductance microscopy—a tool to investigate electrolyte-nonconductor interference. In *Modern Research and Educational Topics in Microscopy*, ed. A Méndez-Vilas, J Díaz, pp. 968–75. Badajoz, Spain: FORMATEX
47. Vinella D, Dari R. 1995. Overview of controls in the *Escherichia coli* cell cycle. *Bioessays* 17:527–36
48. Norbury C, Nurse P. 1992. Animal cell cycles and their control. *Annu. Rev. Biochem.* 61:441–70
49. Gorelik J, Shevchuk AI, Frolenkov GI, Diakonov IA, Lab MJ, et al. 2003. Dynamic assembly of surface structures in living cells. *Proc. Natl. Acad. Sci. USA* 100:5819–22
50. Ubelmann F, Robine S, Louvard D. 2011. Microvilli. In *Cellular Domains*, ed. IR Nabi, pp. 213–28. New York: Wiley
51. Topper JN, Gimbrone MA. 1999. Blood flow and vascular gene expression: fluid shear stress as a modulator of endothelial phenotype. *Mol. Med. Today* 5:40–46



52. Miragoli M, Moshkov A, Novak P, Shevchuk A, Nikolaev VO, et al. 2011. Scanning ion conductance microscopy: a convergent high-resolution technology for multi-parametric analysis of living cardiovascular cells. *J. R. Soc. Interface* 8:913–25
53. Lyon AR, MacLeod KT, Zhang YJ, Garcia E, Kanda GK, et al. 2009. Loss of T-tubules and other changes to surface topography in ventricular myocytes from failing human and rat heart. *Proc. Natl. Acad. Sci. USA* 106:6854–59
54. Ibrahim M, Al Masri A, Navaratnarajah M, Siedlecka U, Soppa GK, et al. 2010. Prolonged mechanical unloading affects cardiomyocyte excitation-contraction coupling, transverse-tubule structure, and the cell surface. *FASEB J.* 24:3321–29
55. Gorelik J, Yang LQ, Zhang YJ, Lab M, Korchev Y, Harding SE. 2006. A novel Z-groove index characterizing myocardial surface structure. *Cardiovasc. Res.* 72:422–29
56. Harding SE, Ali NN, Brito-Martins M, Gorelik J. 2007. The human embryonic stem cell-derived cardiomyocyte as a pharmacological model. *Pharmacol. Ther.* 113:341–53
57. Mann SA, Versmold B, Marx R, Stahlhofen S, Dietzel ID, et al. 2008. Corticosteroids reverse cytokine-induced block of survival and differentiation of oligodendrocyte progenitor cells from rats. *J. Neuroinflamm.* 5:39
58. Gorelik J, Ali NN, Kadir S, Lab M, Stojkovic P, et al. 2008. Non-invasive imaging of stem cells by scanning ion conductance microscopy: future perspective. *Tissue Eng. C* 14:311–18
59. Shin W, Gillis KD. 2006. Measurement of changes in membrane surface morphology associated with exocytosis using scanning ion conductance microscopy. *Biophys. J.* 91:L63–65
60. Smith PR, Bradford AL, Schneider S, Benos DJ, Geibel JP. 1997. Localization of amiloride-sensitive sodium channels in A6 cells by atomic force microscopy. *Am. J. Physiol. Cell Physiol.* 272:1295–98
61. Tousson A, Alley CD, Sorscher EJ, Brinkley BR, Benos DJ. 1989. Immunochemical localization of amiloride-sensitive sodium channels in sodium-transporting epithelia. *J. Cell Sci.* 93:349–62
62. Korchev YE, Negulyaev YA, Edwards CRW, Vodyanoy I, Lab MJ. 2000. Functional localization of single active ion channels on the surface of a living cell. *Nat. Cell Biol.* 2:616–19
63. Fozzard HA. 1977. Heart: excitation-contraction coupling. *Annu. Rev. Physiol.* 39:201–20
64. Coutinho-Silva R, Parsons M, Robson T, Lincoln J, Burnstock G. 2003. P2X and P2Y purinoceptor expression in pancreas from streptozotocin-diabetic rats. *Mol. Cell. Endocrinol.* 204:141–54
65. Dubyak GR. 2003. Knock-out mice reveal tissue-specific roles of P2Y receptor subtypes in different epithelia. *Mol. Pharmacol.* 63:773–76
66. Wong AM, Chow AW, Au SC, Wong CC, Ko WH. 2009. Apical versus basolateral P2Y<sub>6</sub> receptor-mediated Cl<sup>−</sup> secretion in immortalized bronchial epithelia. *Am. J. Respir. Cell Mol. Biol.* 40:733–45
67. Rieg T, Vallon V. 2009. ATP and adenosine in the local regulation of water transport and homeostasis by the kidney. *Am. J. Physiol. Regul. Integr. Comp. Physiol.* 296:419–27
68. Praetorius HA, Leipziger J. 2010. Intrarenal purinergic signaling in the control of renal tubular transport. *Annu. Rev. Physiol.* 72:377–93
69. Zhang YJ, Sanchez D, Gorelik J, Klenerman D, Lab M, et al. 2007. Basolateral P2X<sub>4</sub>-like receptors regulate the extracellular ATP-stimulated epithelial Na<sup>+</sup> channel activity in renal epithelia. *Am. J. Physiol. Renal Physiol.* 292:1734–40
70. Gorelik J, Zhang YJ, Sanchez D, Shevchuk A, Frolenkov G, et al. 2005. Aldosterone acts via an ATP autocrine/paracrine system: the Edelman ATP hypothesis revisited. *Proc. Natl. Acad. Sci. USA* 102:15000–5
71. Nikolaev VO, Moshkov A, Lyon AR, Miragoli M, Novak P, et al. 2010.  $\beta_2$ -Adrenergic receptor redistribution in heart failure changes cAMP compartmentation. *Science* 327:1653–57
72. Potter CMF, Lundberg MH, Harrington LS, Warboys CM, Warner TD, et al. 2011. Role of shear stress in endothelial cell morphology and expression of cyclooxygenase isoforms. *Arter. Thromb. Vasc. Biol.* 31:384–414
73. Sanchez D, Johnson N, Li C, Novak P, Rheinländer J, et al. 2008. Noncontact measurement of the local mechanical properties of living cells using pressure applied via a pipette. *Biophys. J.* 95:3017–27
74. Mann SA, Meyer JW, Dietzel ID. 2006. Integration of a scanning ion conductance microscope into phase contrast optics and its application to the quantification of morphological parameters of selected cells. *J. Microsc.* 224:152–57



75. Korchev YE, Raval M, Lab MJ, Gorelik J, Edwards CRW, et al. 2000. Hybrid scanning ion conductance and scanning near-field optical microscopy for the study of living cells. *Biophys. J.* 78:2675–79
76. Gorelik J, Shevchuk A, Ramalho M, Elliott M, Lei C, et al. 2002. Scanning surface confocal microscopy for simultaneous topographical and fluorescence imaging: application to single virus-like particle entry into a cell. *Proc. Natl. Acad. Sci. USA* 99:16018–23
77. Shevchuk AI, Hobson P, Lab MJ, Klennerman D, Krauzewicz N, Korchev YE. 2008. Endocytic pathways: combined scanning ion conductance and surface confocal microscopy study. *Pflüg. Arch. Eur. J. Physiol.* 456:227–35
78. Shevchuk AI, Hobson P, Lab MJ, Klennerman D, Krauzewicz N, Korchev YE. 2008. Imaging single virus particles on the surface of cell membranes by high-resolution scanning surface confocal microscopy. *Biophys. J.* 94:4089–94
79. Proksch R, Lal R, Hansma PK, Morse D, Stucky G. 1996. Imaging the internal and external pore structure of membranes in fluid: tapping mode scanning ion conductance microscopy. *Biophys. J.* 71:2155–57
80. Kueng A, Kranz C, Mizaikoff B. 2005. Imaging of ATP membrane transport with dual micro-disk electrodes and scanning electrochemical microscopy. *Biosens. Bioelectron.* 21:346–53
81. Kallio T, Slevin C, Sundholm G, Holmlund P, Kontturi K. 2003. Proton transport in radiation-grafted membranes for fuel cells as detected by SECM. *Electrochem. Commun.* 5:561–65
82. Macpherson JV, de Mussy JPG, Delplanck JL. 2002. High-resolution electrochemical, electrical, and structural characterization of a dimensionally stable Ti/TiO<sub>2</sub>/Pt electrode. *J. Electrochem. Soc.* 149:B306–13
83. Still JW, Wipf DO. 1997. Breakdown of the iron passive layer by use of the scanning electrochemical microscope. *J. Electrochem. Soc.* 144:2657–65
84. Haram SK, Bard AJ. 2001. Scanning electrochemical microscopy. 42. Studies of the kinetics and photoelectrochemistry of thin film CdS/electrolyte interfaces. *J. Phys. Chem. B* 105:8192–95
85. Fonseca SM, Barker AL, Ahmed S, Kemp TJ, Unwin PR. 2003. Direct observation of oxygen depletion and product formation during photocatalysis at a TiO<sub>2</sub> surface using scanning electrochemical microscopy. *Chem. Commun.* 2003:1002–3
86. Comstock DJ, Elam JW, Pellin MJ, Hersam MC. 2010. Integrated ultramicroelectrode-nanopipet probe for concurrent scanning electrochemical microscopy and scanning ion conductance microscopy. *Anal. Chem.* 82:1270–76
87. Takahashi Y, Shevchuk AI, Novak P, Murakami Y, Shiku H, et al. 2010. Simultaneous noncontact topography and electrochemical imaging by SECM/SICM featuring ion current feedback regulation. *J. Am. Chem. Soc.* 132:10118–26
88. Ebejer N, Schnippering M, Colburn AW, Edwards MA, Unwin PR. 2010. Localized high resolution electrochemistry and multifunctional imaging: scanning electrochemical cell microscopy. *Anal. Chem.* 82:9141–45
89. Lai SCS, Dudin PV, Macpherson JV, Unwin PR. 2011. Visualizing zeptomole (electro)catalysis at single nanoparticles within an ensemble. *J. Am. Chem. Soc.* 133:10744–47
90. Neher E, Sakmann B, Steinbach JH. 1978. The extracellular patch clamp: a method for resolving currents through individual open channels in biological membranes. *Pflüg. Arch. Eur. J. Physiol.* 375:219–28
91. Bustamante JO, Ruknudin A, Sachs F. 1991. Stretch-activated channels in heart cells: relevance to cardiac hypertrophy. *J. Cardiovasc. Pharmacol.* 17:S110–13
92. Sigurdson W, Ruknudin A, Sachs F. 1992. Calcium imaging of mechanically induced fluxes in tissue-cultured chick heart: role of stretch-activated ion channels. *Am. J. Physiol. Heart Circ. Physiol.* 262:1110–15
93. Green DJ, Gillette R. 1983. Patch-clamp and voltage-clamp analysis of cyclic AMP-stimulated inward current underlying neuron bursting. *Nature* 306:784–85
94. Bossu JL, Feltz A. 1984. Patch-clamp study of the tetrodotoxin-resistant sodium current in group C sensory neurones. *Neurosci. Lett.* 51:241–46
95. Gao YJ, Zhang L, Samad OA, Suter MR, Yasuhiko K, et al. 2009. JNK-induced MCP-1 production in spinal cord astrocytes contributes to central sensitization and neuropathic pain. *J. Neurosci.* 29:4096–108
96. Gorelik J, Gu YC, Spohr HA, Shevchuk AI, Lab MJ, et al. 2002. Ion channels in small cells and subcellular structures can be studied with a smart patch-clamp system. *Biophys. J.* 83:3296–303

97. Dutta AK, Korchev YE, Shevchuk AI, Hayashi S, Okada Y, Sabirov RZ. 2008. Spatial distribution of maxi-anion channel on cardiomyocytes detected by smart-patch technique. *Biophys. J.* 94:1646–55
98. Gu YC, Gorelik J, Spohr HA, Shevchuk A, Lab MJ, et al. 2002. High-resolution scanning patch-clamp: new insights into cell function. *FASEB J.* 16:748–50
99. James AF, Sabirov RZ, Okada Y. 2010. Clustering of protein kinase A–dependent CFTR chloride channels in the sarcolemma of guinea-pig ventricular myocytes. *Biochem. Biophys. Res. Commun.* 391:841–45